Structural, elastic and vibrational properties of celestite, $SrSO_4$, from synchrotron X-ray diffraction, thermal diffuse scattering and Raman scattering

A. Girard, M. Stekiel, D. Spahr, W. Morgenroth, and B. Winkler

Institut für Geowissenschaften, Goethe Universität Frankfurt,

Altenhöferallee 1, D-60438 Frankfurt am Main, Germany

Tra Nguyen-Thanh, A. Bosak, A. Mirone, A. Minelli, and L. Paolasini

ESRF - The European Synchrotron, 71, Avenue des Martyrs, F-38000 Grenoble, France

V. Milman

Dassault Systémes BIOVIA, CB4 0WN Cambridge, United Kingdom

B. Wehinger

Department of Quantum Matter Physics, University of Geneva,

24, Quai Ernest Ansermet, CH-1211 Geneva, Switzerland

(Dated: November 2, 2018)

In order to resolve inconsistencies encountered in published data for $SrSO_4$, the elasticity and the phase stability of celestite has been studied using thermal diffuse scattering, high pressure powder synchrotron X-ray diffraction, Raman scattering and DFT calculations. The structure of $SrSO_4$ is found to be stable up to 62 GPa at ambient temperature. The preferred values for the components of the elastic stiffness tensor have been determined using X-ray thermal diffuse scattering and are (in GPa): c_{11} = 105, c_{22} = 92, c_{33} = 114, c_{44} = 16, c_{55} = 31, c_{66} = 26, c_{12} = 40, c_{13} = 52, c_{23} = 37. The preferred value for the bulk modulus is K=62(2) GPa. This work shows that thermal diffuse scattering collected at two temperatures allows the determination of the full elastic tensor of crystals with low space group symmetry.

PACS numbers: Valid PACS appear here

I. INTRODUCTION

A current pressing problem in the field of the disposal of nuclear waste is the immobilisation of ^{226}Ra ($T_{1/2}$ = 1622 years) which accumulates either as a decay product of ^{238}U or due to the decay of ^{238}Pu via ^{234}U and ^{230}Th in waste repositories [1, 2]. The activity of ^{226}Ra in such a repository will be maximal in about 10^5 years [3], which corresponds to the time where containers may loose their structural integrity [2, 3], implying the possible release of Ra into the environment. Then, geological barriers could still contribute to the immobilization of the radionuclides due to the formation of solid solutions, and hence a significant effort is currently being spent on understanding the thermodynamics of the formation of the relevant solid solutions.

Specifically, if the host rock is a clay, sulfates may play an important role due to the formation of (Ba,Sr,Ra)SO_4 solid solutions and hence considerable effort has been spent in the thermodynamic assessment of such solid solutions [4–8]. However, a prerequisite for the construction and use of thermodynamic models is that the properties of at least the end-members are well constrained. In contrast to $BaSO_4$, several physical properties of $SrSO_4$ are currently debated controversially and the present paper adresses these issues.

$BaSO_4$ and $SrSO_4$ are currently thought to be isostructural (space group *Pnma*), and belong to a group of minerals with the barite structure, where each metal (M) atom is coordinated by 12 oxygen atoms from 6 neighbouring SO_4 tetrahedra, resulting in edge sharing SO_4 and MO_{12} polyhedra [9]. The high pressure elastic and vibrational properties of $BaSO_4$ [10–15] and $PbSO_4$ [12, 16] were studied with Raman and *in situ* X-ray diffraction. For $BaSO_4$ transitions towards the high pressure phases have been reported at ≈10 GPa [12] and between 15 - 27 GPa, depending on the pressure transmitting medium used [13]. However, another X-ray diffraction (XRD) study did not observe any phase transition up to 21 GPa [10].

For $SrSO_4$, Chen et al. [17] reported a high pressure Raman and XRD study up to 24 GPa with a phase transition at 11 GPa and a bulk modulus K = 87 GPa [17]. They reported a very unusual compression behavior of the a-axis, where the pressure dependence shows a minimum before the transition. The inferred transition pressure conspicuously corresponds to the pressure at which a solidification of the 4:1 methanol-ethanol mixture [18] used as pressure transmitting medium in their experiment is expected. More recently, Yunqian et al. [9] reported an *in situ* angle-dispersive X-ray diffraction study where they used an ethanol-methanol-water mixture as transmitting pressure medium [9]. They saw no phase transition and obtained a bulk modulus $K = 62(5)$ GPa, but their study was limited to 15 GPa. The large discrepancy in the values for the bulk modulus of $SrSO_4$ of about 40 % obtained in these two studies from an equation of state and the inconsistent findings concerning the presence of a pressure-induced

structural phase transition are addressed in the present study.

The coefficients of the elastic stiffness tensor, c_{ij}, of $SrSO_4$ were obtained in an ultrasound study by Rao [19] and are given in Tab. III. The bulk modulus obtained from the elastic stiffness tensor was $K = 81.8$ GPa. The values reported in that study [19] for c_{22}, c_{12}, c_{13} and c_{23} differ significantly from those reported for isostructural barite $K_{BaSO_4} = 58.2$ GPa [20] (Tab. III), which is expected to have comparable elastic properties as those of $SrSO_4$. Therefore, we redetermined the elastic stiffness tensor both experimentally and using density functional theory.

Recently, a new method was reported to study the elasticity of crystals from the quantitative analysis of thermal diffuse scattering (TDS), *i.e.* the scattering of X-rays by phonons measured in a single crystal synchrotron diffraction experiment [21]. The method is based on the fit of the TDS intensities due to acoustic phonons in the vicinity of the Bragg reflections, where the fitting coefficients are the elements of the elastic tensor c, namely the elastic stiffness coefficients c_{ij}. If the region of interest (ROI) is chosen such that the elastic approximation is fulfilled, *i.e.* where the acoustic phonons disperse linearly, then absolute values of the elastic stiffness coefficients can be obtained with a model-free data analysis [21], as implemented in TDS2EL [22]. The proposed method is therefore an alternative to other existing techniques commonly used to study elasticity. Its advantage in comparison to Pressure X-Ray Diffraction (PXRD) [23] is that the complete tensor, and not only the bulk modulus, can be determined. In contrast to ultrasound measurements, where samples with well defined faces and minimum size of a few hundreds of μm are required [19], crystals of arbitrary shape as small as a few μm can be investigated with TDS measurements. Furthermore, the new method is suitable for opaque systems as well, which are difficult to measure with Brillouin scattering [24]. Finally, the data collection in a TDS experiment is much faster than typically required for Inelastic X-ray (IXS) or neutron (INS) scattering [25, 26].

If the crystal is of good quality and there is no significant contribution due to elastic diffuse scattering, a TDS measurement at a single temperature (ST) is sufficient to obtain the elastic tensor. In cases where elastic diffuse scattering is observed together with thermal diffuse scattering a "multi-temperature" (MT) approach can be considered, exploiting the fact that the temperature dependence of TDS differs significantly from the temperature dependence of other contributions to diffuse scattering, such as elastic scattering from defects or dislocations. The MT approach is based on the comparison of diffraction patterns measured at two temperatures in the same geometry. The elastic tensor is then obtained from the difference signal, where other contributions to the diffuse scattering are removed by subtraction.

Here, we report a study of the elasticity of $SrSO_4$ using DFT calculations, TDS, PXRD and Raman spectroscopy.

The structural stability under high pressure is reported up to 62 GPa and the proposed structural phase transition reported around 10 GPa is discussed. We address the merits and short-comings of both the "single temperature" and "multi-temperature" TDS methods to obtain the full elastic tensor of $SrSO_4$.

II. METHODS

A. High pressure XRD and Raman scattering

Synthetic $SrSO_4$ from Johnson Matthey with 99.7 % purity was loaded into Boehler-Almax type diamond anvil cells (DACs) for high pressure experiments. Ruby crystals were used as a pressure gauge, by measuring the shift of the fluorescence line. Neon was used as pressure transmitting medium and Re as gasket. The diamond culets had a diameter of 300 μm and an opening angle of 48°. Powder diffraction pattern were collected at the Extreme Conditions Beamline P02.2 at PETRA III, Hamburg, Germany. The general purpose table was used with a beam focused by CRLs to 8 × 2.4 μm^2 (FWHM, H×V) at 42.66 keV (corresponding to 0.29063 Å) and a detector distance of 400 mm. Diffraction images were recorded with a PerkinElmer detector that was calibrated using a CeO_2 powder standard. Powder diffraction data were collected from ambient pressure up to 61.7 GPa. Lattice parameters were retrieved by performing Le Bail fits as implemented in Jana2006 [27]. The bulk modulus values were derived using the EoSFit program [28].

High pressure Raman scattering data were collected with a custom built spectrometer in Frankfurt, which specifications are described elsewhere [29]. Raman spectra were measured upon the decompression of the samples previously measured with X-rays.

Diffuse X-ray scattering data were recorded in transmission geometry on a natural crystal of unknown origin at the ID28 beamline side station from the European Synchrotron Radiation Facility (ESRF). The sample was prepared by mechanical cutting, polishing and etching to minimize the presence of surface defects. Monochromatic X-rays were used with an energy of 15.89 keV (λ = 0.78 Å) and a beam size of 40 × 40 μm^2 (full width at half maximum). Each dataset consists of 3600 images recorded at a sample-detector distance of 244 mm with 0.1° angular step width and 1 second counting time (integration during the rotation, total acquisition time 1 h) with a single photon counting pixel detector. We used a PILATUS 1M detector from Dectris with no readout noise and large dynamical range, equipped with a 300 μm thick Si sensor having pixels of size 172 × 172 μm^2.

B. Thermal diffuse scattering

The quantitative analysis of the thermal diffuse scattering is based on a fit of the three-dimensional distribution of the intensity of scattered x-rays in the vicinity of Bragg reflections [21]. Assuming the adiabatic and harmonic approximation, the intensity of X-rays inelastically scattered from phonons for a single-phonon process is given by:

$$I_1(\mathbf{Q}) = \frac{\hbar N I_{\text{inc}}}{2} \sum_{\nu} \Omega_{\mathbf{q},\nu} \left| \sum_{s} \frac{f_s(\mathbf{Q})}{\sqrt{m_s}} e^{-W_{s,\mathbf{Q}}} (\mathbf{Q}\mathbf{e}_{\mathbf{Q},\nu,s}) e^{-i\mathbf{Q}\tau_s} \right|^2, \tag{1}$$

with

$$\Omega_{\mathbf{q},\nu} = \frac{1}{\omega_{\mathbf{q},\nu}} \coth\left(\frac{\hbar\omega_{\mathbf{q},\nu}}{2k_B T}\right). \tag{2}$$

Here, N is the number of unit cells, I_{inc} the incident beam intensity, and f the atomic scattering factor of ion s with mass m and (anisotropic) Debye-Waller factor W. ω corresponds to the eigenfrequency and $\mathbf{e}$ the eigenvector of the phonon at reduced momentum transfer $\mathbf{q} = \mathbf{Q} - \tau$ and branch ν. $\mathbf{Q}$ is the total scattering vector, τ the atomic basis vector within the unit cell, V the unit cell volume, T the temperature, and k_B the Boltzmann constant. For small values of q the single phonon scattering is dominated by the acoustic phonons with $I_1(\mathbf{Q}) \approx 1/\omega^2_{\mathbf{q},\nu}$.

The elastic stiffness coefficients are obtained from the diffuse intensity in the equation of motion from the theory of elastic waves in crystals [30]:

$$\rho\omega^2 u_i = c_{ijlm} k_j k_l u_m, \tag{3}$$

where $\mathbf{k} = k\mathbf{n}$ and ω are the wave vector and the frequency of the elastic waves, respectively, ρ is the mass density, and c_{ijlm} are the elastic stiffness coefficients. Further information can be found in e.g. Bosak et al. [31], Xu and Chiang [32]. In the case of our $SrSO_4$ crystals, temperature independent diffuse scattering was observed together with thermal diffuse scattering. Therefore, we employed the MT approach to retrieve the elastic tensor.

C. First-principles calculations

First-principles calculations were carried out within the framework of density-functional theory (DFT) [33] and the pseudopotential method as implemented in CASTEP [34]. "On the fly" generated norm-conserving pseudopotentials from the CASTEP data base were employed in conjunction with plane waves up to a kinetic energy cutoff of 990 eV. Most calculations were based on the Wu-Cohen exchange correlation functional [35], while complementary calculations employed the LDA, PBE [36] and a dispersion-corrected PBE functional [37]. A Monkhorst- Pack grid was used for Brillouin-zone integrations with a distance of <0.012 Å^{-1} between grid points. Convergence criteria included an energy change of $<5 \times 10^{-6}$ eV/atom for self consistent field cycles, a maximal force of <0.006 eV/Å, and a maximal component of the stress tensor <0.01 GPa. The latter values are especially tight convergence criteria for low symmetry compounds. Phonon frequencies were obtained from density functional perturbation theory calculations, while elastic stiffness coefficients were computed using stress-strain relations.

III. RESULTS

A. XRD

We have measured X-ray powder diffraction patterns of $SrSO_4$ up to 62 GPa to determine the value of the bulk modulus and its pressure derivative. The experimental diffraction pattern are gathered in Fig. 1a.

All observed reflections could be indexed using space group P*bnm*. The powder was textured, which sometimes caused sudden changes of relative reflection intensities between subsequent measurements. We did not observe any anomaly in the pressure-dependence of the lattice parameters, as shown in Fig. 1b. The dataset was used to determine the values of bulk modulus and its derivative (K and K') at ambient pressure by fitting a 3^{rd} order Birch-Murnaghan equation of state to the data. The volume at ambient conditions was not refined, instead we carried out a precise measurement using $SrSO_4$ powder outside a diamond anvil cell under the same conditions. Results are shown in Fig. 2. As observed by Yunqian et al. [9], there is a high negative correlation between K and K' values, depicted in Fig. 2b using ellipsoidal contour lines of $\chi^2_w(K,K')$ for different confidence levels. The different values reported for K and K' values are summarized in Table I together with the results of the present study. These values are compared to the ones obtained from our calculations, either from the c_{ij} or by fitting our theoretical compression curve. The theoretical values obtained by the two methods are in good agreement with the experimental result.

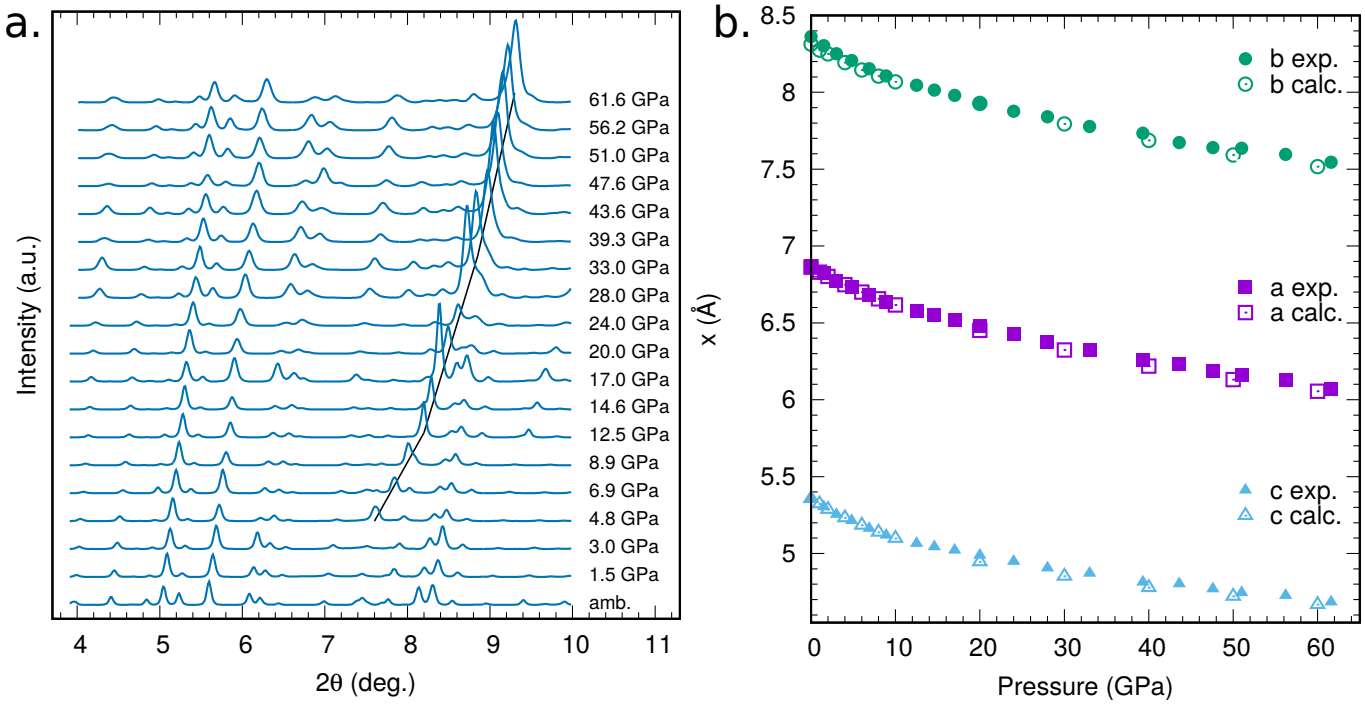

FIG. 1. a. Powder diffraction pattern of $SrSO_4$ at high pressure. Reflection marked with a black line comes from solid neon. The pattern are vertically shifted for clarity. b. Evolution of the lattice parameters of $SrSO_4$ with applied pressure, as determined from Le Bail fits of the experimental patterns.

TABLE I. Comparison of the bulk modulus of $SrSO_4$ obtained from high pressure XRD (PXRD), DFT calculations and TDS with literature data.

K (GPa)	K'	Ref.	comment
61 (7)	6 (1)	this study	PXRD, Ne as pressure medium
61.7 (1.1)	-	this study	DFT from c_{ij}
67 (8)	5 (1)	this study	DFT from EoS.
63	-	this study	TDS
62 (5)	11 (1)	[9]	PXRD, 16:3:1 meth.-eth.-water
98 (2)	4 (fixed)	[9]	PXRD, 16:3:1 meth.-eth.-water
87 (3)	4 (fixed)	[17]	PXRD, 4:1 methanol-ethanol
83	4 (fixed)	[38]	PXRD

B. Lattice dynamics

We have measured the Raman scattering signal of $SrSO_4$ from ambient conditions up to 50 GPa. In Fig.3 we compare the experimental and calculated Raman spectra at ambient pressure conditions. The calculated Raman shifts were multiplied by 1.05 in order to compensate the systematical underbinding occurring in General Gradient Approximation based DFT calculations. Both the positions and the intensities of the peaks are correctly reproduced, except for the 459 cm^{-1} peak corresponding to the bending of the SO_4 tetrahedra. This mode is split in the calculations and is overlapping in the measurement. Additionally, the lowest frequency calculated mode is not present in our experimental Raman spectra because it is cut out by the Notch filter of our spectrometer. The pressure dependence of the Raman

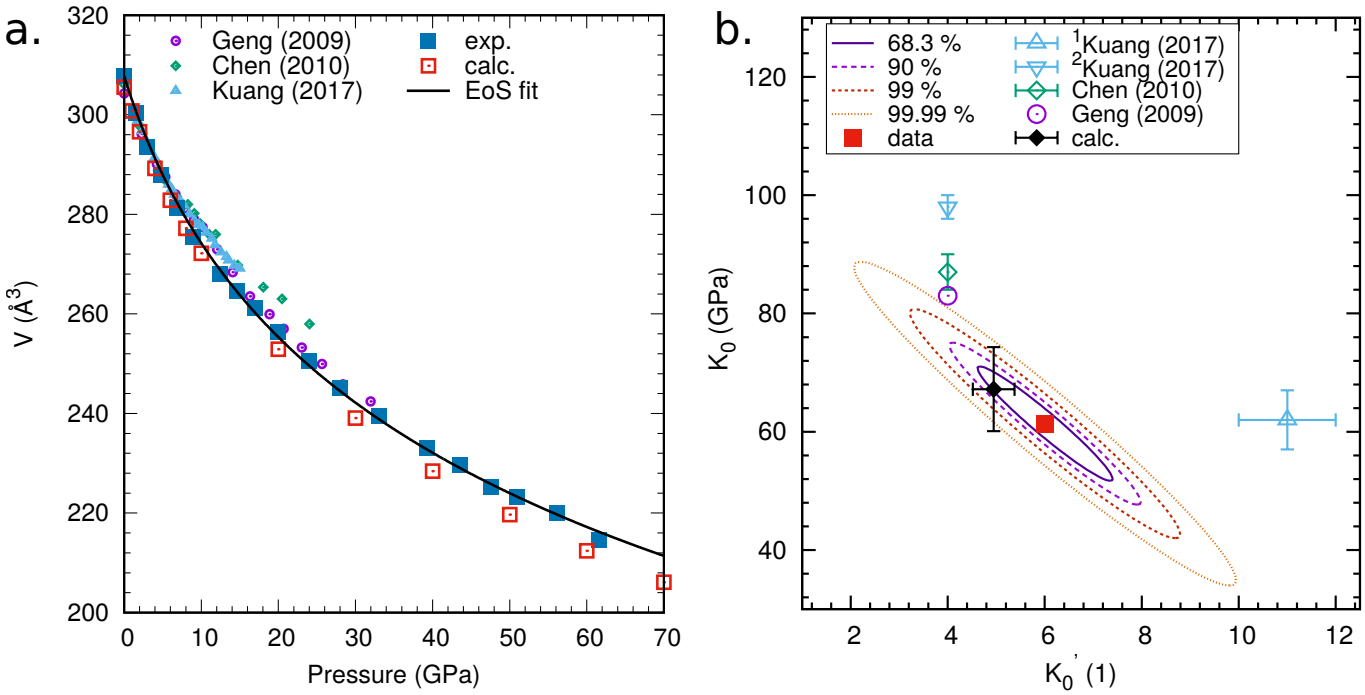

FIG. 2. a. Pressure dependence of the unit cell volume measured (full dark blue squares) and calculated (empty red squares) in this study, together with the data from Geng et al. [38] (empty purple circles), Chen et al. [17] (empty green diamonds) and Yunqian et al. [9] (empty light blue triangles). The black line shows the fit to the experimental data. b. Bulk modulus (K_0) versus bulk modulus derivative (K_0') values from the PXRD measurement in this study (empty black square) along with the values reported by other authors (see panel b. legend and Table I). Dashed lines present confidence ellipses for the fit of K_0 and K_0' to the measured V(p) relation. The DFT value (from c_{ij}) is shown as a black diamond.

spectra is shown in Fig. 4.a and b. At high pressures only the most intense modes could be resolved. The peak at 460 cm^{-1} splits to two modes at 7.6 GPa (see Fig. 4.a and b), however our calculations show that these modes were incidentally overlapping at ambient pressure. At around 30 GPa a shoulder appears upon increasing pressure on the low wavenumber side of the most intense peak. Again our calculations show that this is due to incidental overlap of two modes at lower pressures. No other splitting nor an appearance of a new mode was observed.

C. DFT calculations

In an earlier study [8] we noticed that in large super-cell calculations a full geometry optimisation led to slight deviations from the orthorhombic symmetry, but this was not explored further. Similar calculations carried out here reproduced the result and the structure shown in Vinograd et al. [8], where the SO_4-groups are slightly rotated in comparison to the orthorhombic structure (Fig. 5).

Here, we computed the lattice dynamics for the orthorhombic structure and noted two Γ-point phonons with slightly imaginary (-40i and -13i cm^{-1}) frequencies (sign is positive, imaginary frequencies result from square root of a negative

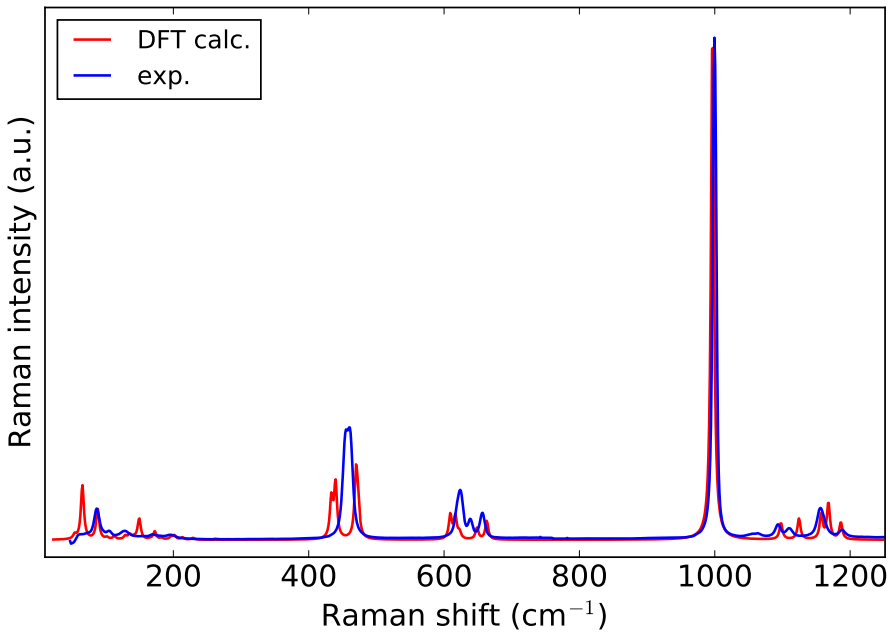

FIG. 3. Measured (blue) and calculated (red) Raman spectra of $SrSO_4$ at ambient pressure.

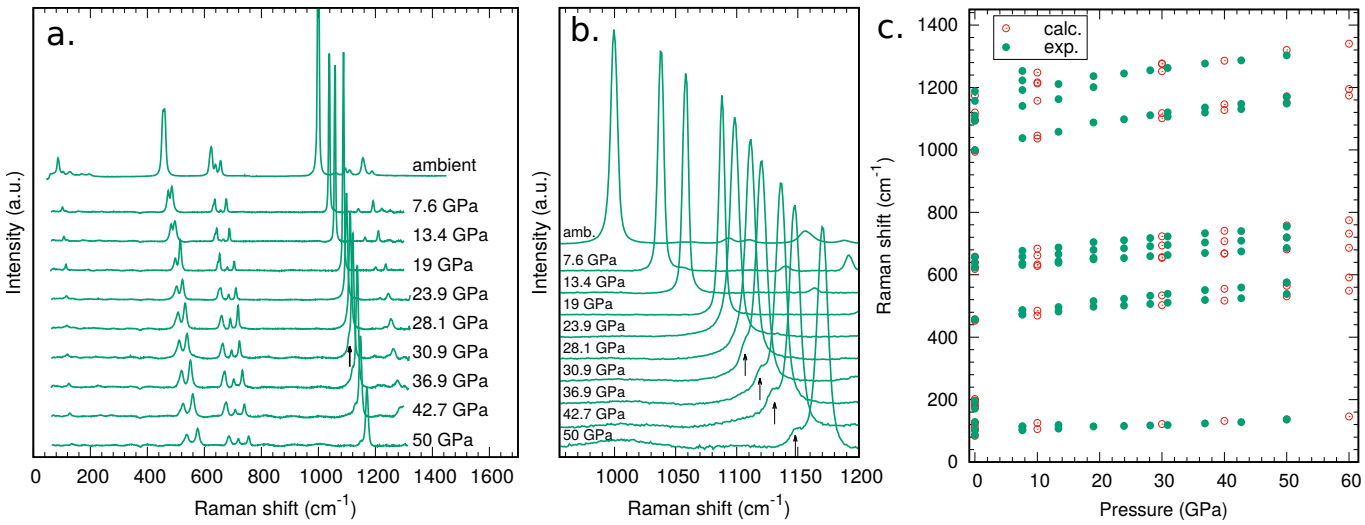

FIG. 4. a. Raman spectra measured at high pressures. The arrows indicates the phonon mode that appears as a shoulder above 7.6 GPa (see text). b. Magnified view of the region where peak overlap occurs. c. Pressure dependence of the Raman active modes from measurement (full green circles) and DFT calculations (empty red circles).

number). A distortion of the structure according to the polarisation vector of the lowest frequency phonon with a subsequent full geometry optimisation and symmetry analysis led to a structure with space group $P2_1/n$, where we use the unconventional setting in order to facilitate a comparison of the lattice parameters, given in Table II. For this structure, all frequencies are real.

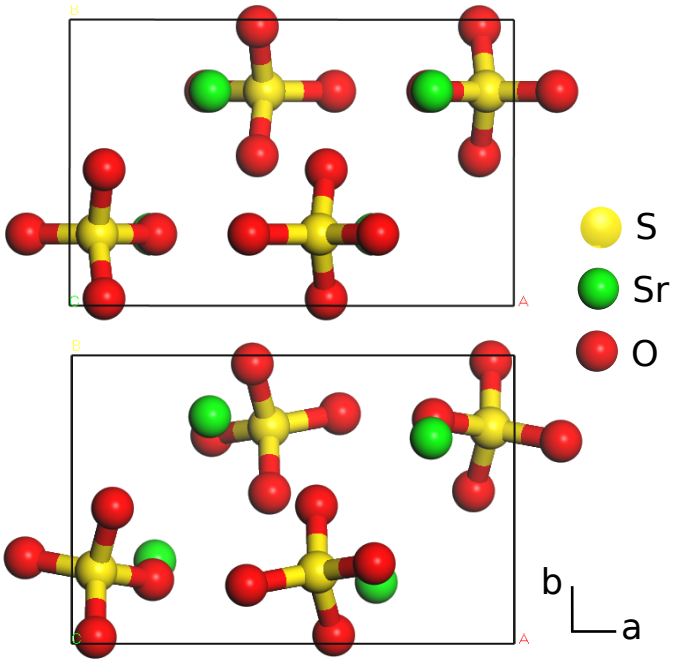

FIG. 5. Full geometry optimisations with tight convergence criteria lead, independent of the *xc*-functional employed, to a monoclinic ground state structure (bottom), in which the SO_4-tetrahedra are slightly rotated with respect to their orientation in the orthorhombic structure (top).

	exp.	DFT	DFT
	P*nma*	P*nma*	P$2_1/n$
a (Å)	8.354	8.3136	8.2945
b (Å)	5.359	5.3365	5.3990
c (Å)	6.862	6.8501	6.8778
α (°)	90.0	90.0	90.86

TABLE II. Lattice parameters of $SrSO_4$ obtained from T = 100 K experimental diffraction data and DFT calculations in the P*nma* and P$2_1/n$ space groups.

The monoclinic polymorph is slightly more stable (by ≈ 0.07 eV per formula unit) than the orthorhombic structure. This is independent of the exchange-correlation functional used - we tested this with the local density approximation, PBE, dispersion-corrected PBE and Wu-Cohen exchange-correlation functionals, with full geometry optimization. A monoclinic angle deviating by ≈ 1° from 90° could be resolved experimentally. However, due to the very small energy differences, it is more likely that even at low temperatures the SO_4-tetrahedra would be either statically or dynamically disordered, leading to an overall orthorhombic structure.

The components of the elastic stiffness tensor are very similar for the orthorhombic and monoclinic structure. In comparison to the elastic stiffnes tensor of the orthorhombic strucure (Table III), the monoclinic tensor has four more non-zero components (c_{15} = 0.8(2) GPa, c_{25} = 0.2(2) GPa, c_{35} = 3.5(3) GPa, c_{46} = 4.0(5) GPa. The bulk moduli differ only slightly (monoclinic: 57.6(3) GPa, orthorhombic: 62(1) GPa). These results allowed us to employ the

tensor for the orthorhombic structure in the subsequent discussion. On pressure increase, the monclinic form becomes unstable, and above 4 GPa the orthorhombic form is the stable polymorph.

D. Thermal diffuse scattering

First, the elastic constants were obtained using the "single temperature" method at $T_1 = 100$ K. We fitted the diffuse intensity in the vicinity of the 29 most intense reflections. The region of interest (ROI) were defined by the reduced wavevector $q_i = \Delta Q_i / |\mathbf{a^*}|$, and the fitted data belonged to the regions where $q \in [q_{\min}, q_{\max}]$ with $q_{\min} = 0.06$, $q_{\max} = 0.2$. The regions above $q_{\max}$ were excluded in order to fit only the part of reciprocal space were the elastic approximation is valid. The regions below $q_{\min}$ were excluded to avoid the contamination by elastic scattering in the vicinity to the Bragg peaks.

Measured and theoretical TDS intensities in selected cuts of reciprocal space are shown in Fig. 6 for the single temperature method at $T_1 = 100$ K. For the fit, images containing Bragg peaks were removed [39]. The elastic coefficients obtained from the fit are gathered in Table III. The elastic tensor c was obtained using a single scaling factor with the ST approach and the absolute values result from the rescaling to our theoretical c_{11} value, according to the previously established procedure [21]. In Table III we compare the elastic coefficients of $SrSO_4$ derived from the ST approach to those obtained by DFT calculations. Most of the fitted elastic coefficients obtained with the ST method are in good agreement with the theoretical values, except for the c_{44}, c_{66} and c_{13} coefficients. The ST approach is sensitive to any elastic contribution to the diffuse scattering, arising from defects, dislocation or disorder.

In order to disentangle the elastic and inelastic contributions to the diffuse scattering, one possibility is to use energy and momentum resolved measurements. To this end, Inelastic X-ray Scattering (IXS) available at ID28 beamline can provide additional insights about structural disorder by analysing the intensity of the zero–energy–transfer line. The intensity of the central line is weak when the crystal is of good quality, and increases in the presence of defects, thereby providing a qualitative estimate of the defect state of the sample. In the case of $SrSO_4$, the elastic contribution was confirmed by the presence of a strong central line in the IXS spectra of our sample (not shown here), indicating the presence of defects or structural disorder. This is consistent with a local disorder of the SO_4 tetrahedra, as deduced from the DFT calculations. Therefore, the deviations observed in the fitted elastic stiffness coefficients relative to the calculated values likely stem from the contribution of elastic diffuse scattering.

The determination of the elastic tensor c based on the single temperature measurement is based on the assumption that the diffuse signal originates from the acoustic phonons only. In cases where a small elastic component is present,

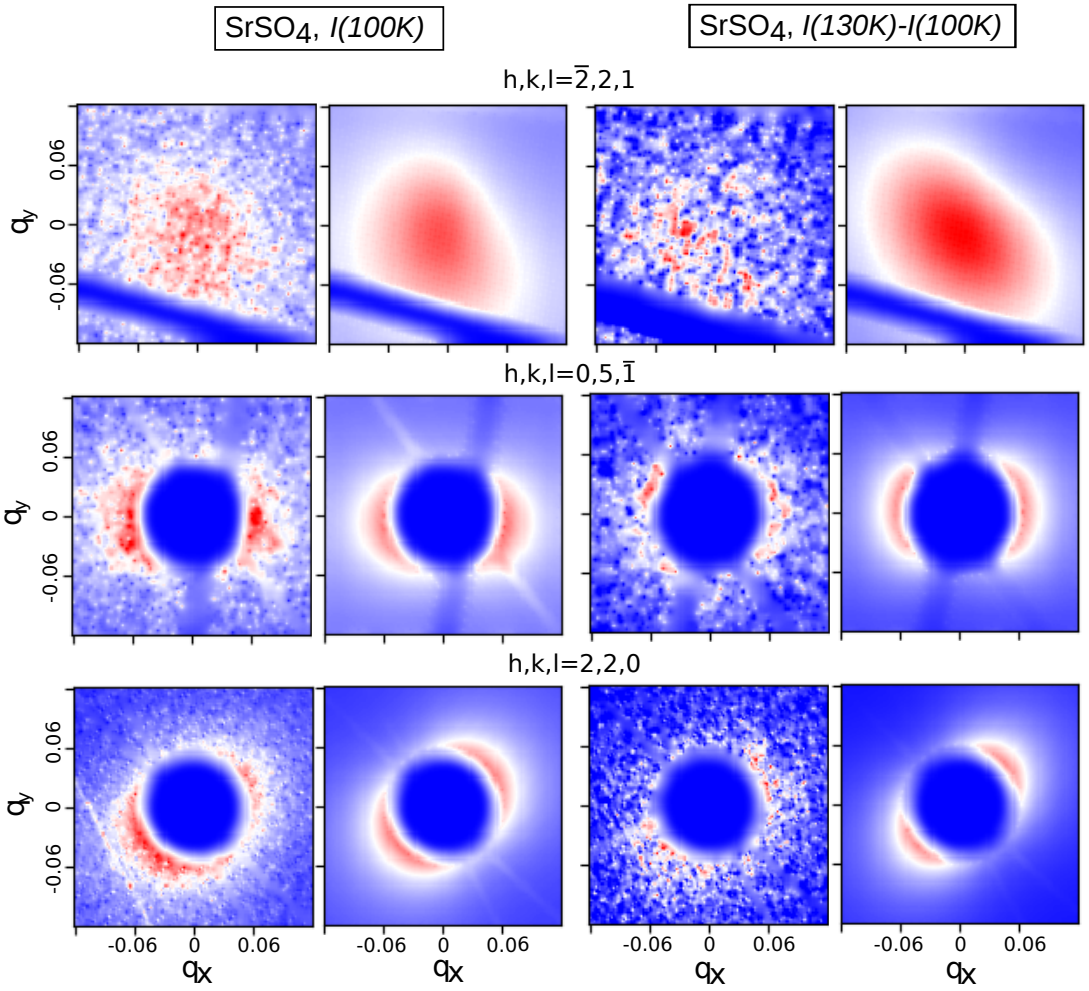

FIG. 6. Graphical rendering of experimental diffuse scattering and calculated TDS for $SrSO_4$. Left panel: measurements at $T = 100$ K with ROI of $q \in [0.06, 0.2]$ and right panel: MT approach at $T = 100$, 130 K. The data are grouped by pairs, with experimental patterns on the left-hand side and the calculated ones on the right-hand side. The images show cross sections of reciprocal space near a selection of Bragg reflections. The intensity is plotted on a linear color scale from blue (zero) to red (maximal intensity $I_{\max}$). The stripes with zero intensity are due to the removal of some frames containing saturated/defective pixels in the data processing.

				$SrSO_4$				$BaSO_4$
	DFT	Ultrasound	Rel. diff.	TDS: ST	Rel. diff.	TDS: MT	Rel. diff.	Ultrasound
	this work	Ref. [19]		this work		this work		Ref. [20]
c_{11}	107.0 (2.2)	104	2.8 %	107	-	104	2.8 %	95.14 (0.08)
c_{22}	90.7 (4.3)	106	16.8 %	94	3.6 %	95	4.7 %	83.65 (0.08)
c_{33}	116.0 (3.7)	129	11.2 %	111	4.5 %	112	3.6 %	110.6 (0.08)
c_{44}	17.7 (1.0)	13.5	31.1 %	45	254 %	18	1.7 %	11.81 (0.05)
c_{55}	41.0 (1.0)	27.9	46.9 %	37	10.8 %	35	17.1 %	29.03 (0.06)
c_{66}	25.8 (3.0)	26.6	3.1 %	16	61.3 %	26	0.7 %	27.66 (0.06)
c_{12}	41.6 (2.1)	77	85.1 %	39	6.7 %	39	6.7 %	51.32 (0.15)
c_{13}	49.4 (1.8)	60	21.4 %	29	70.3 %	54	9.3 %	33.62 (0.12)
c_{23}	35.0 (2.0)	62	77.1 %	34	2.9 %	40	14 %	32.76 (0.12)

TABLE III. Elastic coefficients of $SrSO_4$ in GPa obtained from DFT calculations and TDS analysis with the ST ($T_1 = 100$ K) and the MT methods ($T_1 = 100$ K, $T_2 = 130$ K). The elastic coefficients were fitted in both cases in the ROI $q \in [0.06, 0.2]$. For the ST set, the values were rescaled to the calculated value of c_{11}. The values for $BaSO_4$ are also reported for comparison. Relative differences (Rel. Diffs.) are the relative deviation of the experimental coefficients with respect to our DFT calculations.

i.e. the diffuse scattering does not originate from the phonons only, an alternative option is to obtain the elastic tensor c from the difference between two measurements at different temperatures. Because the temperature dependence of diffuse scattering from static disorder is much weaker than the one due to the phonon scattering, it can be subtracted using patterns acquired at two different temperatures T_1 and T_2 in the same geometry. The results of the fit of c from TDS patterns resulting from the temperature subtraction of two datasets measured at $T_1 = 100$ K and $T_2 = 130$ K are reported in Table III.

In Fig. 6 we show a graphical rendering of the experimental and fitted temperature-differentiated TDS patterns, for the same set of Bragg reflections shown for the ST approach, where the same ROI were employed. The data are necessarily more noisy but of sufficient quality to obtain a reliable fit of the diffuse scattering intensities. The temperatures were chosen such that the probed ROI corresponds to acoustic phonons satisfying the condition $\hbar\omega > k_B T$. In these conditions, the intensities measured at T_1 and T_2 which compare to the Bose factor $\coth(\hbar\omega/k_B T)$, become linearly independent. Therefore the temperature determines the scale to which ω scale. Absolute values of the elastic coefficients can be obtained if the probed ROI corresponds to the region where the elastic approximation is fulfilled.

The elastic coefficients obtained using the MT method are summarized in Table III along with their relative difference with the calculated values. The agreement for the c_{44}, c_{66} and c_{13} coefficients is now very satisfactory due to the elimination of the elastic contribution in the subtraction procedure. Apart from the c_{55} and the c_{23} coefficients which show relative difference of 17.1 % and 14 % with the calculations respectively, all coefficients show less than 10 % relative difference, and the quality of the fit is confirmed by the comparison of the experimental and calculated TDS patterns. The obtained values of the elastic coefficients were used to obtain the bulk modulus $K_{TDS} = 63$ GPa, which is gathered together with the calculated value, the value obtained from compression data in this study and other literature data in Table I.

IV. DISCUSSION

The bulk modulus values derived in this study can be used to evaluate previously published data [9, 17, 38], see Table I. Scatter of the values reported earlier might be due to different pressure ranges covered in each study, as well as the pressure transmitting media used. As shown in a similar study on barite, $BaSO_4$ [13], performing the high-pressure experiments with unsuitable pressure transmitting media results in systematic errors. Chen et al. [17] used a methanol-ethanol mixture as the pressure medium and Yunqian et al. [9] used a methanol-ethanol-water mixture.

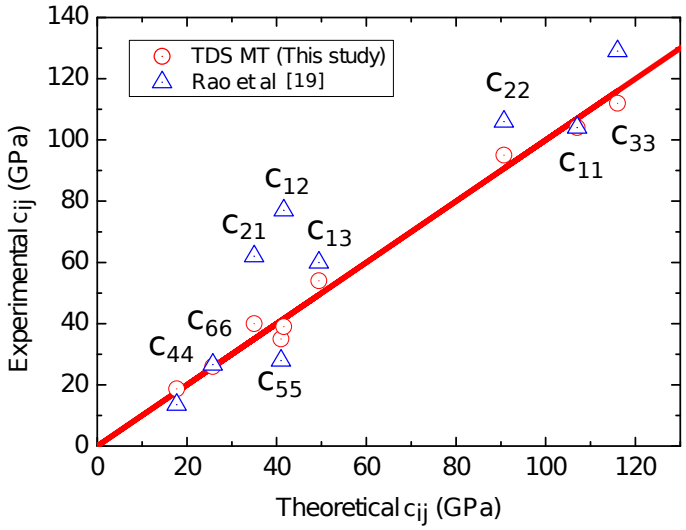

FIG. 7. Elastic stiffness coefficients of $SrSO_4$ obtained from TDS (this study) and ultrasound [19] plotted against calculated values (this study).

Both substances solidify at 10 GPa, and at pressures above 10 GPa yield a significant pressure gradient in the DAC sample chamber, leading to non-hydrostatic conditions and inaccurate pressure determinations. As shown by Klotz et al. [18], at 20 GPa this pressure gradient is an order of magnitude higher for the mixtures used by Chen et al. [17] and [9] than for neon used in this study. In contrast, the bulk modulus values derived in this study by three independent methods, namely DFT calculations: K_{DFT} = 61.7 (1.1) GPa from the C_{ij} and K_{DFT} = 67 (8) GPa from the theoretical EoS, TDS: K_{TDS} = 63 GPa and compression data: K_{PXRD} = 61.4 (6.4) GPa are mutually in very good agreement. Therefore the preferred value for the bulk modulus of $SrSO_4$ is $K = 62(2)$ GPa and $K' = 6(1)$.

Some of the elastic stiffness coefficients for $SrSO_4$ obtained here from TDS and DFT calculations are in rather poor agreement with reported data from earlier ultrasound measurements [19]. c_{11}, c_{44} and c_{66} are in good agreement within a few percent for all three data sets. However, the values given by Rao [19] for c_{22}, c_{33} and c_{55} differ by more than 12 GPa from our values and the off-diagonal components c_{12}, c_{13} and c_{23} given by Rao [19] are approximately 1.5 times larger than the values obtained here. For the sake of comparison, these values are gathered in Table III together with the experimental data for $BaSO_4$ and are compared to values obtained here in Fig. 7. The differences between TDS, DFT and ultrasound elastic tensors are also shown in Fig. 8. It corresponds to the representation surfaces of the longitudinal part of the elastic stiffness tensor calculated based on the set of elastic coefficients provided by the three different methods. Clearly, the DFT- and TDS-derived data are in very good mutual agreement, as is typical for comparisons between c_{ij} derived from experiment and those obtained from calculations [24, 41–43]. Another way to qualitatively assess the correctness of a set of c_{ij} coefficients is to compare the shape of the measured TDS

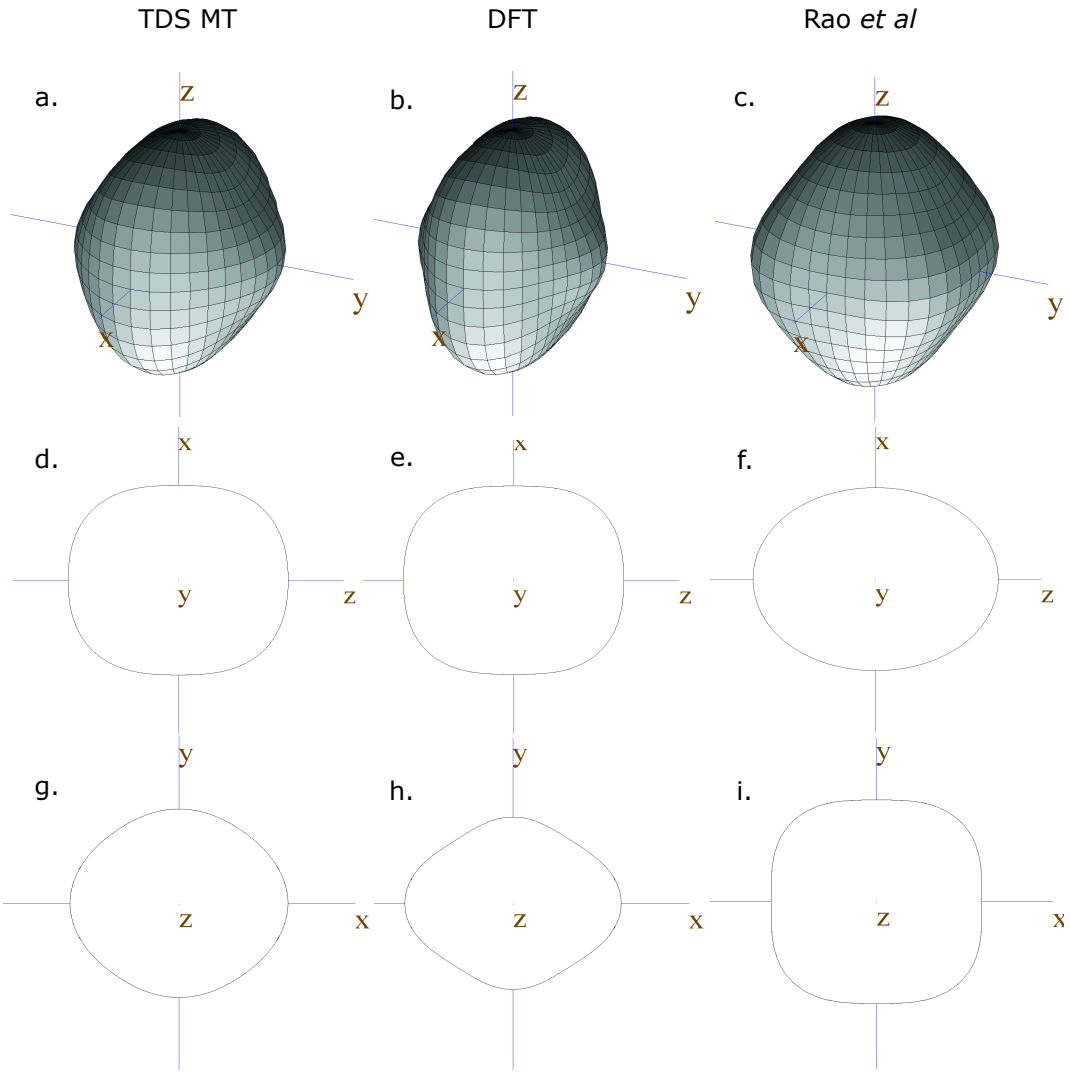

FIG. 8. Representation surfaces of the longitudinal elastic effect in $SrSO_4$ calculated based on the elastic stiffness coefficients obtained with a. TDS, b. DFT and c.ultrasound from left to right. Top panels show 3D representation surfaces, middle and bottom panels correponds to 2D cuts in the xz (d., e., f.) and xy (g., h., i.) planes respectively. The tensor representations were obtained using the wintensor program [40].

in high symmetry planes with the calculated TDS (without fitting). Fig. 9 shows the experimental TDS intensity distributions of $SrSO_4$ in 0KL and HK0 planes around the 020 Bragg reflection, which are compared to the calculated TDS based on c_{ij} obtained from our DFT calculations and the ultrasound experiments by Rao *et al* [19]. First we notice that the butterfly shape obtained from the ultrasound data in the HK0 plane is in poor agreement with the results based on either DFT or experimental data, which better agree with each other. Second we notice a widening of the neck of the butterfly shape in the experimental data, which is typical of a contribution from elastic diffuse scattering. This is in agreement with the failure of the ST method for the fitting of the c_{ij}. A further indication, that the data from Rao [19] need to be revised comes from the comparsion to $BaSO_4$. The elastic properties of $BaSO_4$ and $SrSO_4$ are expected to be similar, and clearly our $SrSO_4$ data is very similar to the data for $BaSO_4$ published by

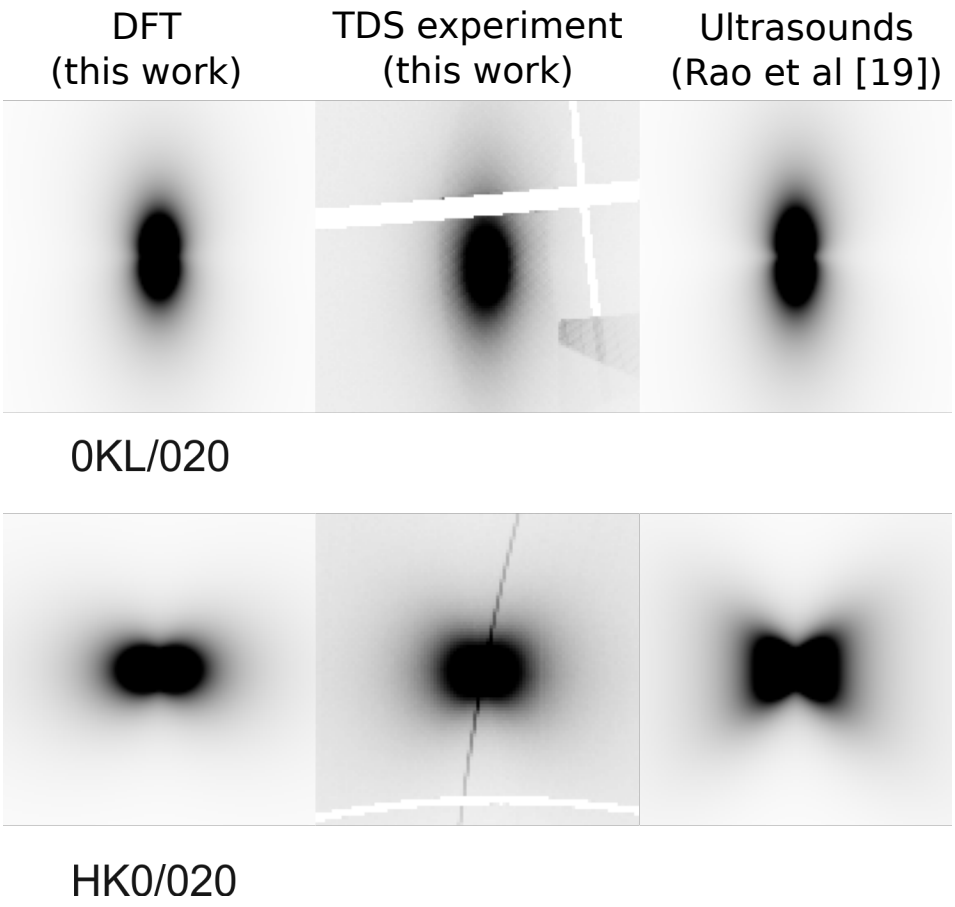

FIG. 9. Experimental TDS intensity distributions of $SrSO_4$ in 0KL (top) and HK0 (bottom) planes around 020 Bragg reflection (this work, middle panels), compared to the calculated TDS based on c_{ij} obtained from DFT calculations (this work, left panels) and ultrasound experiments (Rao *et al* [19], right panels).

Haussühl [20]. Hence we conclude that a preferred set of data is (in GPa): $c_{11} = 105$, $c_{22} = 92$, $c_{33} = 114$, $c_{44} = 16$, $c_{55} = 31$, $c_{66} = 26$, $c_{12} = 40$, $c_{13} = 52$, $c_{23} = 37$. For c_{55} our results where underweighted, as the value for $BaSO_4$ is significantly smaller and in agreement with the result by Rao [19].

As discussed by Yunqian et al. [9] the phase transition of $SrSO_4$ at 10 GPa reported by Chen et al. [17] is likely an artefact. We have not observed any anomaly in the dependence of lattice parameters on pressure up to 62 GPa. Our Raman scattering data show some peak splitting with pressure, which were related by our calculations to an incidental overlapping of Raman modes at lower pressures. We have not observed significant changes in the slope of Raman modes frequencies with pressure. Our combined Raman and XRD results thus ascertain that no pressure-induced phase transition occurs for celestite up to 62 GPa.

The determination of the elastic stiffness coefficients from TDS fit using the ST method was unsatisfactory in the present case due to an elastic component of the diffuse scattering. In contrast, the MT approach provided a set of coefficients in very good agreement with our calculated values (Table III).

In the case of $SrSO_4$ their are nine independent elastic coefficients to be fitted simultaneously together with the background. This is significantly higher than the two benchmark systems previously studied with this method: calcite (six values) and MgO (three values) [21]. The ST method was used successfully for calcite, where the crystal was of very high quality. In the case of MgO, the MT method was used, but as only three coefficients needed to be determined the sensitivity of the fit to the low signal intensity was not a problem. Hence, the current demonstration that the MT approach can also be used to obtain a reliable elastic tensor for crystal symmetries involving a high number of elastic stiffness coefficients is a significant advancement. In the present case, we used a temperature interval $\Delta T = T_2$ - T_1 = 30 K. In future studies, it will be interesting to measure at many temperatures with small intervals and increased statistics. This will allow us to address the temperature dependence of the elastic moduli, see discussion in Ref. [21].

In summary, we have investigated the structure and vibrational properties of celestite, $SrSO_4$, at high pressure from X-ray powder diffraction and Raman scattering and its elastic stiffness tensor from the analysis of X-ray TDS in the vicinity of the most intense Bragg reflections. Our high pressure data allowed to undoubtedly invalidate the debated structural transition around 10 GPa, where reported changes in compression are likely due to non-hydrostatic conditions induced by the transmitting pressure medium. Additionally, the phase stability of $SrSO_4$ was demonstrated up to 62 GPa. The quantitative analysis of the thermal diffuse scattering, which could be isolated by a temperature difference measurement, allowed to obtain a reliable elastic stiffness tensor for $SrSO_4$ in good agreement with our DFT calculations. The elastic coefficients and bulk modulus obtained by three independent methods, namely DFT calculations, TDS and PXRD, agree well with each other, and allowed to rationalize the discrepancies found in the literature. Finally, the MT method is shown to allow the extraction of a number of elastic stiffness coefficients as high a nine in the present case with an orthorhombic symmetry. Thus, the combination of TDS analysis from a single crystal synchrotron diffraction experiment and DFT calculations is shown to be a rapid and efficient alternative to other constraining methods such as IXS, Brillouin spectroscopy or ultrasound measurements.

V. ACKNOWLEDGEMENTS

This study was supported by the BMBF projects 05K13RF2, 05K13RF1, 05K13RF2, 05K13RFA, 05K13RFB and a joint DFG-ANR project WI1232/41-1. Parts of this research were carried out at the light sources ESRF (Grenoble, France) PETRA III at DESY (Hamburg, Germany). We would like to thank Hanns-Peter Liermann and his team for assistance in using beamline P02.2. We thank Denis Gambetti for technical support in the operation of ID28 beamline of the ESRF.

[1] F. Grandia, J. Merino, and J. Bruno. Assessment of the radium-barium co-precipitation and its potential Influence on the solubility of Ra in the near-field. Technical Report TR- 0807, Svensk Kärnbränsle-hantering AB. Swedish Nuclear Fuel and Waste Management Company, Sweden, 2008.

[2] NAGRA. An Assessment of the Corrosion Resistance of the High-level Waste Containers Proposed by NAGRA. Technical Report TR-84–32, The Nagra Working Group on Container Technology, December 1984.

[3] SKB. Long-term safety for the final repository for spent nuclear fuel at Forsmark. Main report of the SR-Site project Volume III. Technical Report TR-11–01, Svensk Kärnbränslehantering Ab. 563–893, ISSN 1404–0344, March 2011.

[4] E. Curti, K. Fujiwara, K. Iijima, J. Tits, C. Cuesta, A. Kitamura, M. A. Glaus, and W. Müller. Radium uptake during barite recrystallization at 23 ± 2°C as a function of solution composition: An experimental ^{133}Ba and ^{226}Ra tracer study. *Geochimica et Cosmochimica Acta*, 74(12):3553–3570, 2010. ISSN 0016-7037. doi: https://doi.org/10.1016/j.gca.2010.03.018.

[5] V. L. Vinograd, F. Brandt, K. Rozov, M. Klinkenberg, K. Refson, B. Winkler, and D. Bosbach. Solid-aqueous equilibrium in the $BaSO_4$–$RaSO_4$–H_2O system: First-principles calculations and a thermodynamic assessment. *Geochimica et Cosmochimica Acta*, 122:398–417, 2013. ISSN 0016-7037. doi:https://doi.org/10.1016/j.gca.2013.08.028.

[6] Y. O. Rosenberg, Y. Sadeh, V. Metz, C. M. Pina, and J. Ganor. Nucleation and growth kinetics of $Ra_xBa_{1-x}SO_4$ solid solution in NaCl aqueous solutions. *Geochimica et Cosmochimica Acta*, 125:290–307, 2014. doi:10.1016/j.gca.2013.09.041.

[7] V. L. Vinograd, D. A. Kulik, F. Brandt, M. Klinkenberg, J. Weber, B. Winkler, and D. Bosbach. Thermodynamics of the solid solution – Aqueous solution system (Ba,Sr,Ra)SO_4 + H_2O: II. Radium retention in barite-type minerals at elevated temperatures. *Applied Geochemistry*, 2017. ISSN 0883-2927. doi:https://doi.org/10.1016/j.apgeochem.2017.10.019.

[8] V. L. Vinograd, D. A. Kulik, F. Brandt, M. Klinkenberg, J. Weber, B. Winkler, and D. Bosbach. Thermodynamics of the solid solution – Aqueous solution system (Ba,Sr,Ra)SO_4 + H_2O: I. The effect of strontium content on radium uptake by barite. *Applied Geochemistry*, 89:59–74, 2018. ISSN 0883-2927. doi:https://doi.org/10.1016/j.apgeochem.2017.11.009.

[9] Kuang Yunqian, Xu Jingui, Zhao Dongyu, Fan Dawei, Li Xiaodong, Zhou Wenge, and Xie Hongsen. The high-pressure elastic properties of celestine and the high-pressure behavior of barite-type sulphates. *High Temperatures – High Pressures*, 46(6):481 – 495, 2017. ISSN 00181544.

[10] W. A. Crichton, M. Merlini, M. Hanfland, and H. Müller. The crystal structure of barite, $BaSO_4$, at high pressure. *American Mineralogist*, 96(2–3):364–367, 2011. ISSN 0003004X. doi:10.2138/am.2011.3656.

[11] J. M. Chourot, A. Le Bail, and D. Chevalier. Phase diagram of aqueous solution at high pressure and low temperature. *High Pressure Research*, 19(1–6):191–199, Sep 2000. ISSN 0895-7959. doi:10.1080/08957950008202554.

[12] Pei Lun Lee, Eugene Huang, and Shu Cheng Yu. High-pressure Raman and X-ray studies of barite, $BaSO_4$. *High Pressure Research*, 23(4):439–450, 2003. ISSN 08957959. doi:10.1080/0895795031000115439.

[13] D. Santamaría-Pérez, L. Gracia, G. Garbarino, A. Beltrán, R. Chuliá-Jordán, O. Gomis, D. Errandonea, Ch Ferrer-Roca, D. Martínez-García, and A. Segura. High-pressure study of the behavior of mineral barite by x-ray diffraction. *Physical Review B - Condensed Matter and Materials Physics*, 84(5):1–8, 2011. ISSN 10980121. doi:10.1103/PhysRevB.84.054102.

[14] Yen-Hua Chen, Eugene Huang, and Shu-Cheng Yu. High-pressure Raman study on the $BaSO_4$ – $SrSO_4$ series. *Solid State Communications*, 149(45–46):2050–2052, 2009. ISSN 00381098. doi:10.1016/j.ssc.2009.08.023.

[15] E. Goldish. X-Ray diffraction analysis of barium-strontium sulfate (barite–celestite) solid solutions. *Powder Diffraction*, 4 (4):214–216, 1989. ISSN 19457413. doi:10.1017/S0885715600013750.

[16] Pei-Lun Lee. High-Pressure Raman Study on Anglesite. *World Journal of Condensed Matter Physics*, 03(01):28–32, 2013. ISSN 2160-6919. doi:10.4236/wjcmp.2013.31005.

[17] Yen-Hua Chen, Shu-Cheng Yu, Eugene Huang, and Pei-Lun Lee. Raman spectroscopy and X-ray diffraction studies on celestite. *Physica B: Condensed Matter*, 405(20):4386–4388, 2010. ISSN 09214526. doi:10.1016/j.physb.2010.08.001.

[18] S. Klotz, J.-C. Chervin, P. Munsch, and G. Le Marchand. Hydrostatic limits of 11 pressure transmitting media. *Journal of Physics D: Applied Physics*, 42(7):75413, 2009. doi:10.1088/0022-3727/42/7/075413.

[19] T. Seshagri Rao. Elastic constants of barytes and celestite. *Proceedings of the Indian Academy of Sciences – Section A*, 33(5):251, 1951. ISSN 0370-0089. doi:10.1007/BF03173258.

[20] S. Haussühl. Elastic and thermoelastic properties of isotypic $KClO_4$, $RbClO_4$, $CsClO_4$, $TlClO_4$, NH_4ClO_4, $TIBF_4$, $NH4BF_4$ and $BaSO_4$. *Zeitschrift fur Kristallographie*, 192(1–2):137–145, 1990. ISSN 0044-2968. URL `https://www.degruyter.com/view/j/zkri.1990.192.issue-1-4/zkri.1990.192.14.137/zkri.1990.192.14.137.xml`.

[21] B. Wehinger, A. Mirone, M. Krisch, and A. Bosak. Full Elasticity Tensor from Thermal Diffuse Scattering. *Phys. Rev. Lett.*, 118(3):35502, Jan 2017. doi:10.1103/PhysRevLett.118.035502.

[22] A. Mirone and B. Wehinger. http://ftp.esrf.fr/scisoft/TDS2EL/index.html, 2017.

[23] J. B. Burt, N. L. Ross, R. J. Angel, and M. Koch. Equations of state and structures of andalusite to 9.8 GPa and sillimanite to 8.5 GPa. *American Mineralogist*, 91(2–3):319, 2006. doi:10.2138/am.2006.1875.

[24] N Biedermann, B Winkler, S Speziale, H J Reichmann, and M Koch-Müller. Single-crystal elasticity of $SrCO_3$ by Brillouin spectroscopy. *High Pressure Research*, 37(2):181–192, 2017. doi:10.1080/08957959.2017.1289193.

[25] B. Wehinger, A. Bosak, S. Nazzareni, D. Antonangeli, A. Mirone, S. L. Chaplot, R. Mittal, E. Ohtani, A. Shatskiy, S. Saxena, S. Ghose, and M. Krisch. Dynamical and elastic properties of $MgSiO_3$ perovskite (bridgmanite). *Geophysical Research Letters*, 43(6):2568–2575, 2016. ISSN 1944-8007. doi:10.1002/2016GL067970. 2016GL067970.

[26] M. Stekiel, T. Nguyen-Thanh, S. Chariton, C. McCammon, A. Bosak, W. Morgenroth, V. Milman, K. Refson, and B. Winkler. High pressure elasticity of $FeCO_3$–$MgCO_3$ carbonates. *Physics of the Earth and Planetary Interiors*, 271:

57–63, 2017. ISSN 0031-9201. doi:https://doi.org/10.1016/j.pepi.2017.08.004.
[27] V. Petricek, M. Dusek, and L. Palatinus. Crystallographic Computing System JANA2006: General features. *Zeitschrift für Kristallographie*, 229(5):345–35, 2014. ISSN 2194-4946. doi:10.1515/zkri-2014-1737.
[28] J. Angel Ross and J. Gonzalez-Platas. Eosfit7c and a fortran module (library) for equation of state calculations. *Zeitschrift fur Kristallographie - Crystalline Materials*, 229(5):405–419, 2014.
[29] L. Bayarjargal, C.-J. Fruhner, N. Schrodt, and B. Winkler. $Caco_3$ phase diagram studied with raman spectroscopy at pressures up to 50GPa and high temperatures and DFT modeling. *Physics of the Earth and Planetary Interiors*, 281:31 – 45, 2018. ISSN 0031-9201. doi:https://doi.org/10.1016/j.pepi.2018.05.002.
[30] F. I. Fedorov. *Theory of Elastic Waves in Crystals*. 1968.
[31] A. Bosak, D. Chernyshov, B. Wehinger, B. Winkler, M. Le Tacon, and M. Krisch. In-between Bragg reflections: Thermal diffuse scattering and vibrational spectroscopy with x-rays. *Journal of Physics D: Applied Physics*, 48:504003, 2015. ISSN 0022-3727. doi:10.1088/0022-3727/48/50/504003.
[32] Ruqing Xu and Tai C. Chiang. Determination of phonon dispersion relations by X-ray thermal diffuse scattering. *Zeitschrift fur Kristallographie*, 220(12):1009–1016, 2005. ISSN 00442968.
[33] P. Hohenberg and W. Kohn. Inhomogeneous electron gas. *Phys. Rev.*, 136:B864–B871, Nov 1964. doi: 10.1103/PhysRev.136.B864.
[34] S. J. Clark, M. D. Segall, C. J. Pickard, P. J. Hasnip, P. M. J. Probert, K. Refson, and M. C. Payne. First principles methods using CASTEP. *Z. Kristallogr.*, 220:567–570, 2005.
[35] Zhigang Wu and R. E. Cohen. More accurate generalized gradient approximation for solids. *Phys. Rev. B*, 73:235116, 2006.
[36] John P. Perdew, Kieron Burke, and Matthias Ernzerhof. Generalized gradient approximation made simple. *Physical review letters*, 77:3865–3868, 11 1996. doi:10.1103/PhysRevLett.77.3865.
[37] A Tkatchenko and M Scheffler. Accurate molecular van der waals interactions from ground-state electron density and free-atom reference data. *Phys. Rev. Lett.*, 102:073005, Feb 2009. doi:10.1103/PhysRevLett.102.073005. URL `https://link.aps.org/doi/10.1103/PhysRevLett.102.073005`.
[38] A. H. Geng, Y. M. Ma, M. Li, F. F. Li, and Q. L. Cui. *Mol atoms Phys.*, 26:753, 2009.
[39] I. B. Ramsteiner, A. Schops, H. Reichert, H. Dosch, V. Honkimaki, Z. Zhong, and J. B. Hastings. High-energy X-ray diffuse scattering. *Journal of Applied Crystallography*, 42(3):392–400, 2009. ISSN 00218898. doi:10.1107/S0021889809011492.
[40] Wintensor program. `http://cad4.cpac.washington.edu/wintensorhome/wintensor.html`.
[41] B. Winkler and V. Milman. Density functional theory based calculations for high pressure research. *Zeitschrift für Kristallographie – Crystalline Materials*, 229():112, 2014. doi:10.1515/zkri-2013-1650.
[42] T. Nguyen-Thanh, A. Bosak, J. D. Bauer, R. Luchitskaia, K. Refson, V. Milman, and B. Winkler. Lattice dynamics and elasticity of $SrCO_3$. *Journal of Applied Crystallography*, 49(6):1982–1990, 2016. doi:10.1107/S1600576716014205.
[43] B. B. Karki, L. Stixrude, and R. M. Wentzcovitch. Highpressure elastic properties of major materials of earth's mantle from first principles. *Reviews of Geophysics*, 39(4):507–534, 2001. doi:10.1029/2000RG000088.